

# A Mathematical Model of a Rod Photoreceptor Population

Louis Joslyn

*LSA Math REU Program, University of Michigan*

---

## Abstract

Abstract: Phototransduction is a complex biological process in which photons are detected in the retina giving rise to a meaningful representation of incident light. In low-light conditions, this occurs primarily in the rods with the light signal encoded in their membrane potentials. The ionic current model of Kamiyama et al. (1996 and 2009) describes changes in the rod membrane potential due to a photocurrent and other ionic currents. In the retina, rods function together in a large coupled population. In this work, we simulate a population of rods coupled with gap junctions and study the consequences of the network properties of the coupling. In particular, we consider rods uniformly distributed on a Cartesian grid or hexagonally tilted with varying connection strengths. We examine the biochemistry described by the Kamiyama rod model, present results on our population model, and provide speculation into the functional purpose of gap junctions.

---

## 1. Introduction

Incident light spurs a vertebrate photoreceptor to activate a phototransduction cascade. Phototransduction is a complex biological process that signals the beginning of vision. Photons are detected by the retina and then transformed into a meaningful representation of light. In low-light conditions, this transformation occurs primarily in rods; light signals are encoded in the membrane potential of each rod ([1], [2]). The phototransduction process and flow of photocurrent has been extensively researched and modeled in vertebrate rod photoreceptors ([3], [4], [5]).

Now, the membrane potential of a rod is not determined exclusively by the photocurrent. Ionic currents in the inner segment and current flowing

through gap junctions with other nearby rods contribute to the magnitude of voltage response by each rod ([6]). Researchers have also modeled the inner segment ionic currents ([7], [8], [9], [10]).

However, gap junctions and their role in eyesight have received less attention. In vertebrate retina, gap junctions electrically couple photoreceptors ([11], [12], reviewed in [13]). This coupling allows passage of current to adjacent rods; thus gap junctions play an important role in vision. Prior research suggests that gap junctions improve the signal-to-noise ratio of the photoreceptor output ([14], [3], [15]).

In 2014, Guo et al.([16]) reviewed the major computational models of the retina. While the single rod photoreceptor has been modeled extensively ([9], [4], [17], [18], [19]), current literature lacks a computational model that enables rod interaction across a large population. Using a conductance based rod cell model provided by Kamiyama et al. ([8],[10]), we create a rod population model which yields several compelling results on rod interaction within a network and the physiological function of gap junctions. Specifically, we provide three significant contributions to the literature. First, we transform the single rod cell model proposed by Kamiyama ([8]) into a population model of roughly 500 cells. Second, we constructed the population hexagonally, and show that this anatomically correct structure is preferable to the standard Cartesian layout. Finally, and most importantly, we draw conclusions about the effect of gap junction coupling on eyesight.

## 2. The Single Cell Model

Kamiyama et al. ([8]) used a parallel conductance model to describe the electrical properties, ionic currents and light sensitive current. A detailed description of the ionic current model of the vertebrate rod photoreceptor is listed in Appendix A. Figure 1 shows a circuit model of a photoreceptor. This figure was originally presented by Kamiyama et al.[8].

Figure 2, also originally displayed in Kamiyama et al. [8], shows the dynamics of the intracellular calcium system of the photoreceptor model. The differential equation system located in Appendix A describes how free calcium is diffused and buffered within the submembrane and intracellular central space. The calcium mechanisms of the model are very detailed – the detail is a central reason we selected the single cell model as foundation for our population model.

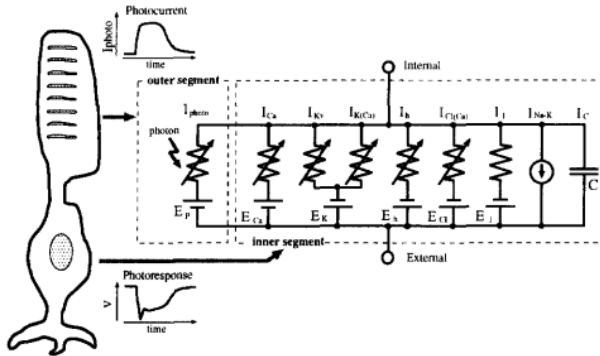


Figure 1: An electrical circuit representation of the Kamiyama Single Cell Ionic Current model. Note that this is a Hodgkin&Huxley style model; each current is evaluated, added together and then divided by membrane capacitance to calculate membrane potential with respect to time.

The photocurrent model presented in Kamiyama et al. [10] can also be found in Torre et al. [4], whom offer the model of phototransduction in retinal rods. The model is included in Appendix A as well. While other phototransduction models are available in the literature we preferred Torre et al.'s model for two reasons. First, Torre et al. provided one of the first quantitative phototransduction models. Consequently, many contemporary models are derived from their basic model structure. Second, for our purposes, we desire a model that can accurately reproduce a photocurrent. We therefore proceed with this pioneer model but added several features that advance the model; namely, we created a population structure that holds many single cell models within it.

The system of differential equations was solved using ode15s, the Matlab (Ver. 14, Mathworks) numerical integrator. Its a stiff systems integrator and was preferable to ode23 or ode45.

### 2.1. Evaluation of Single Cell Model

Figure 3 shows our replication of previous results was successful ([10]). We have accurately reproduced the first figure in Kamiyama et al. [10]. This figure shows photocurrent, photovoltage, and other ionic current responses to a series of light flashes. By reproducing these results, we demonstrated proper replication of the model dynamics and parameters.

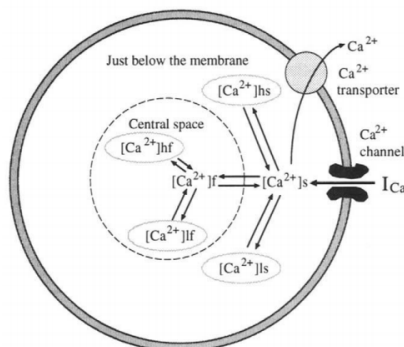


Figure 2: A visual representation of the intracellular calcium system in the single cell model. The rate of change of submembrane calcium concentration ( $[Ca^{2+}]_s$ ) is dependent on inflow of calcium ions ( $I_{Ca}$ ), transport into the central space and binding to low affinity ( $[Ca^{2+}]_{lf}$ ) and high affinity ( $[Ca^{2+}]_{hf}$ ) buffers. Free calcium in the central space ( $[Ca^{2+}]_f$ ) is dependent on high affinity ( $[Ca^{2+}]_{hf}$ ) and low affinity ( $[Ca^{2+}]_{lf}$ ) buffers.

Secondly, we investigated the role of Kamiyama et al.'s  $J_{hv}$  variable. This variable represents the light input to the rod cell in activated rhodopsin per second ( $Rh^*/s$ ). Specifically, we examined the relationship between  $J_{hv}$  and membrane voltage (the output of the model) as shown in Figure 4. Notice that the voltage response is a sigmoidal showing hyperpolarization of the membrane potential with increased light input. Steady output was achieved after 40 seconds of light. Figure 4 represents the steady state voltage depolarization value given a constant input of light. Notice that  $J_{hv}$  was given across several magnitudes of light. This model is an accurate representation of the rod photoreceptor; rods will hit their response threshold when light intensity is too strong. The relationship between  $J_{hv}$  and membrane voltage thus exhibits a saturating response.

We also performed a full sensitivity analysis of the model parameters. Given an input light value of 1000  $Rh^*/s$ , we perturbed each individual parameter by a coefficient of 0.001 and recorded the change in voltage. Table 2.1 shows the effects of these parameter manipulations on membrane potential. Note that the parameters holding the most weight over the output are reversal potentials. In particular, the hyperpolarization activation reversal potential most contributes to voltage response when the input is 1000  $Rh^*/s$ . The hyperpolarization activated current has been shown to contribute significantly to the recovery time after rod hyperpolarization ([7], [10], [10]). Moreover, with a perturbation at one percent, a resultant change in volt-

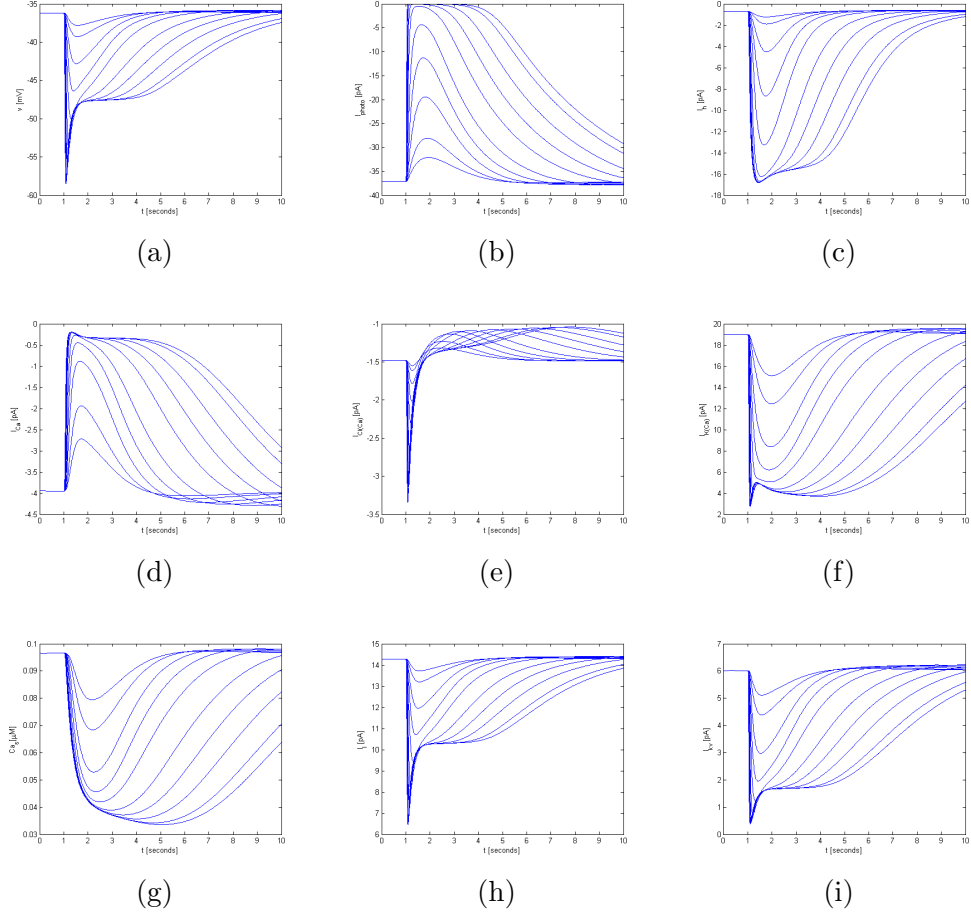


Figure 3: The reproduced first figure from Kamiyama et al. ([10]) using our replication of their model. The stimuli consisted of 20 ms flashes starting at time 1.0 s. The intensities were 1, 2, 5, 10, 10, 50, 100, 200, 500, and 1000  $\text{Rh}^*/\text{s}$ . (a) shows the photoresponse of the rod, (b) shows the photoresponse of the rod created by the phototransduction process, and (c) displays the hyperpolarization activated current. The rest are shown as follows: (d) the Calcium current, (e) Calcium activated chloride current, (f) Calcium activated potassium current, (g) rate of change of shell calcium with respect to time (h) Leakage current (i) potassium current that acts as a delayed rectifier.

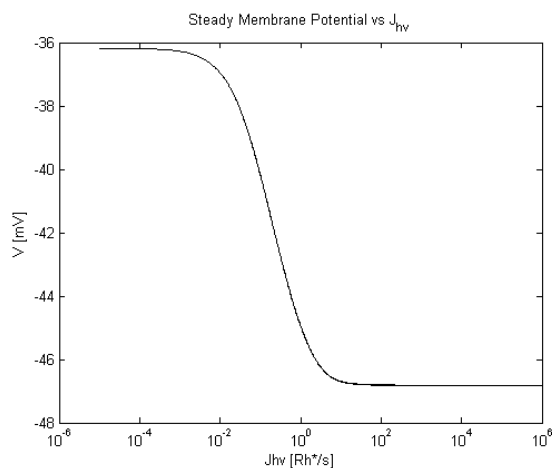


Figure 4: A plot showing the relationship between the input and output of the model.  $J_{hv}$  is shown in logs of light (in  $Rh^*/s$ ) and Voltage is in milliVolts.

age of less than 0.2 mV demonstrates a stable model: no one parameter contributes too significantly to the output.

Parameter	Impact on Voltage
E_h	0.1752
E_l	0.1604
E_k	6.9400E-2
g_l	6.2600E-2
Cl_h	2.6201E-2
g_kc	1.4501E-2
g_kv	1.09E-2
c_0	5.8999E-3
ca_e	5.0001E-3
E_cl	4.7996E-3

Table 1: The top ten parameters that contribute most to voltage response. Each parameter was individually manipulated by .1% and the resulting voltage response was recorded. The change in voltage is shown in the second column. Normally 1000  $Rh^*/s$  create a steady voltage response of  $-46.9305$  mV.

### 3. Population Structure

Several previous contributions to rod networks align rods in a Cartesian layout ([15], [10]). For this particular population structure, every cell has four neighbors. There exists a cell above, below, left and right of the ON-center rod cell. An exception exists for cells along the boundaries of the population. These cells have three neighbors. Figure 5 shows our Cartesian grid of rods.

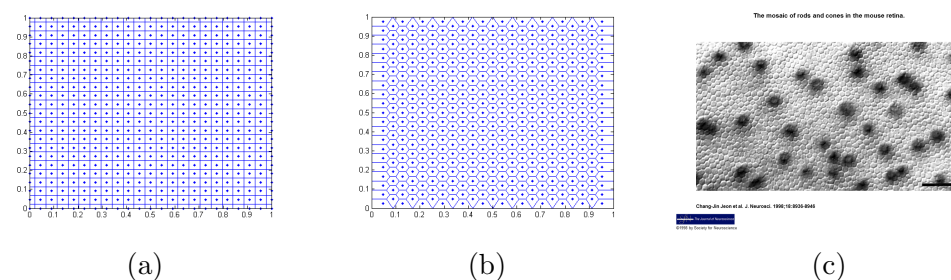


Figure 5: (a) shows the traditional Cartesian layout for rod population models. (b) shows the hexagonal structure we created for our model. (c) shows a rod and cone mosaic from Jeon et al. [20]. The cones are the dark spots, whereas the rods are the more or less polygonal white shapes. Note how (b) is similar in layout to the mosaic.

However, mosaics of the photoreceptor layer in the retina reveal rods are organized in a honeycomb pattern. In the pursuit of a more biologically and anatomically correct model, we distributed our cells in a hexagonal manner, following the model nature provides in mosaics of the retina. Every cell now has six adjacent cells, except those along the boundaries of the population. These cells have either three or four neighbors, depending on their placement along the boundary. Figure 5 shows our hexagonal population structure.

Both Hexagonal and Cartesian population simulations were performed using Matlab (Mathworks).

### 4. Results and Discussion

As in previous research, we first arranged the cells onto a Cartesian grid. Each cell was individual; there was no coupling and therefore no communication of ionic currents among the population. We interpolated a greyscale image of the Mona Lisa onto various cell population sizes to better understand individual rod reaction within a population. Without coupling, each

reaction should depend solely on the light input for each rod. Figure 6 shows the result of this interpolation; each image is presented next to our interpretation. Notice, our representation of the Mona Lisa shows dark pixels along the coordinates that are actually brightest in the photo. For example, the face and chest are the brightest aspects of the image, but our representation shows these areas as the darkest. This is purposeful. We wished to accurately represent rod cell behavior upon an encounter with light. Because rod cells hyperpolarize upon photon absorption, we reproduced our image with the darkest areas representative of the cells which most hyperpolarized upon seeing the photo.



(a) 64 cell population.

(b) 121 cell population.



(c) 256 cell population.

(d) 529 cell population.

Figure 6: Non-coupled, Cartesian structure model population representation of the Mona Lisa image. Note that the image becomes clearer as we model larger numbers of cells.

Similarly, the representation image clarity of our hexagonally structured population hinged on the number of cells we modeled. However, we can directly compare the result of the two population structures. Figure 7 shows

the differences. While both representations are built with uncoupled rod populations just over 500 cells, the hexagonal structure portrays a clearer representation. In fact, the hexagonal representation includes the eyes of the Mona Lisa. Clearly, hexagonal tiling offers the best available option for acute modeling of rod cell reaction.

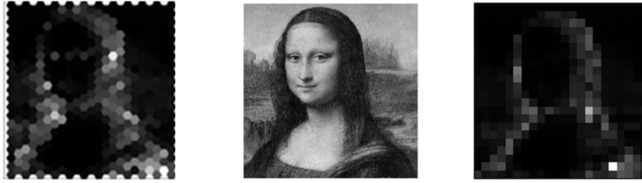


Figure 7: A comparison of the Cartesian and Hexagonal population structures. The representation on the left is hexagonally built, whereas the representation on the right is built using a Cartesian structure.

#### 4.1. Gap Junction Coupling

As stated earlier, our research goal was to determine the contribution of gap junctions to the visual process.

Gap junction coupling was coded by creating a large matrix,  $G$ , of gap junction conductances.  $G_{gap}$  is a variable that holds the gap junctional conductance (nS) between neighboring rods  $i$  and  $j$  in the  $G$  matrix at the position  $G_{i,j}$ . For simplicity, we originally assumed  $G_{gap}$  value was uniform across all neighboring rods.

Intuitively, gap junctions appear contradictory to clear vision. Since rods encode incident light intensity within their membrane potential and gap junctions average neighboring cell voltages, this could cause issues in vision. For example, imagine the visual process that occurs upon seeing a white bar in

front of a black background. Each rod is responsible for encoding a specific point in the image. Rods responsible for encoding the edges of the white bar are particularly important. Gap junctions allow the rods responsible for encoding the white bar edge to communicate ionic currents with rods encoding the black background. Predictably, this could blur the edges of the white bar. We can assume this type of image distortion is not beneficial for sight. Figure 8 shows the effect of various levels of gap junction coupling strength on image representation. As coupling becomes stronger, rods present an increasingly blurry image to the bipolar cells.

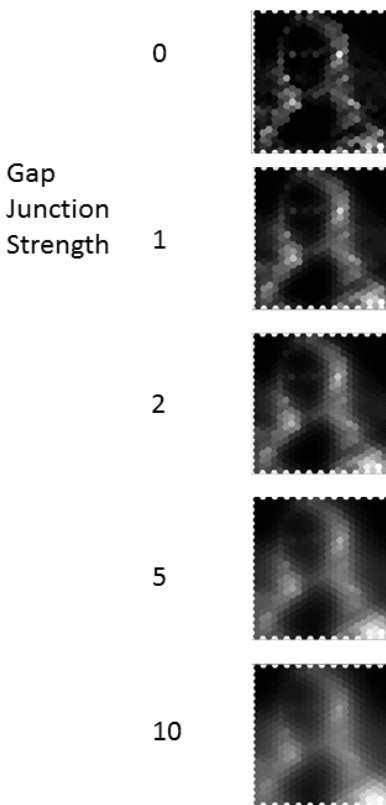


Figure 8: As  $G_{gap}$  value (nS) increases, the representation of the Mona Lisa becomes increasingly blurry.

We recognized parameter uniformity across the population of cell models was biologically inaccurate, as no two cells across biology are precisely the same in all dimensions. Concurrently, we recognized that gap junction

coupling improves the signal to noise ratio in electrical signaling in dim light conditions ([14],[3], [15]). We theorize that gap junction coupling can also contribute to improved signal to noise ratio when noise is caused by parameter variation across the population of retinal rods. Thus, we manipulated every parameter across a Gaussian distribution of several different coefficients of variation. Parameter variation did not encompass spatial structure. Figure 9 shows an array of image representations presented by a rod population of 512 cells. Rows are arranged according to rising  $G_{gap}$  strength and columns are arranged along several different Gaussian distributions. While images at the extremes are extraordinarily pixelated or blurry, we find that the image indexed at the second row and second column may offer the best signal to noise ratio.

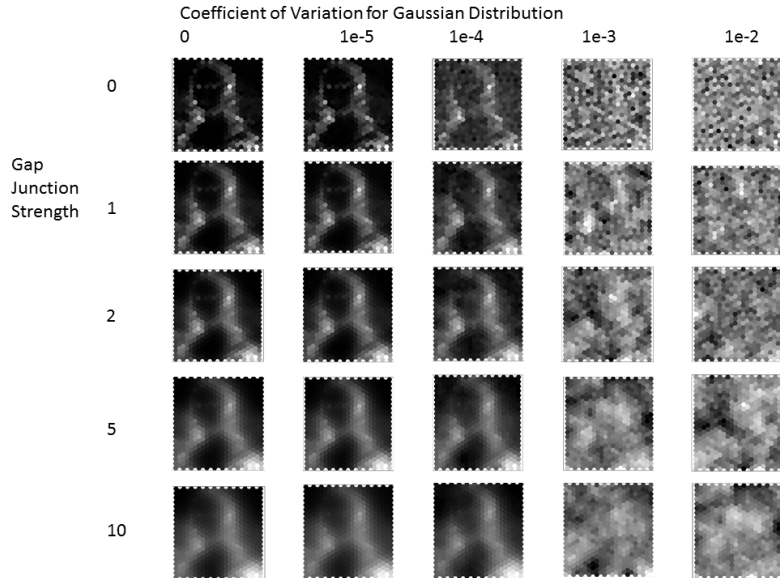


Figure 9: An array of Mona Lisa representations from a hexagonally structured, 512 cell population. Gap Junction strength (nS) increases along the row and coefficient of variation increases across the columns. Note that  $1e - 2$  equals 1% of variation for each parameter.

At best, Figure 9 offers an impression of the effect gap junctions and parameter variation hold on rod response. However, we want to quantitatively and concretely prove that noise due to parameter variation is abated through gap junction coupling. Figure 10 exhibits the empirical relationship between coupling and parameter noise.

Figure 10 shows a histogram of the steady state membrane voltage values

from individual rods whose parameters were manipulated according to a 10% Gaussian variation when exposed to a continual stream of light (1000 Rh\*/s). Now, without parameter variation, these rods should return the same voltage output because they all receive the same, constant level of light input. Due to parameter variation, voltage values range from -28 to -40 mV across the uncoupled population. However, once we introduce coupling, we see voltage values only range from -34 mV to -36 mV. Thus, we have evidence that coupled rods nearly nullify the effect of noise due to parameter variation in photovoltage response.

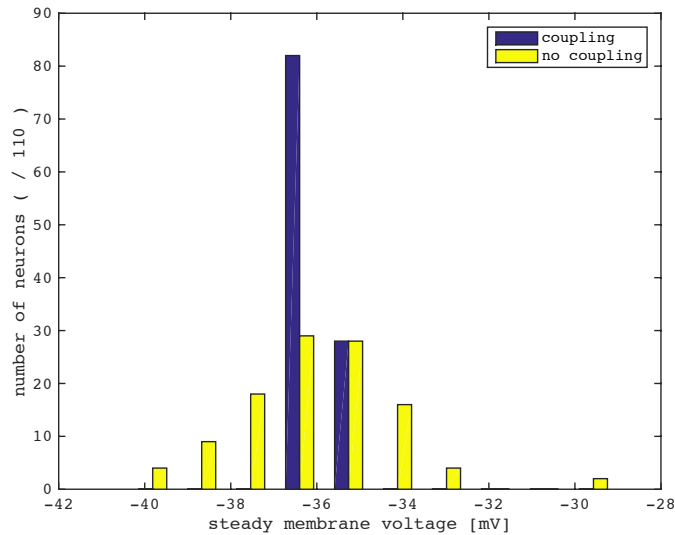


Figure 10: A histogram displaying the effects of coupling (in blue) and no coupling (in yellow). When parameters are distributed throughout the population according to a Gaussian variation of 10%, coupling clearly shortens the range of membrane voltage output. Each rod received a uniform light input of 1000 Rh\*/s

#### 4.2. Weakness and Assumptions

Clearly, results of our population model hinge on characteristics of the individual cell model. Thus, deficiencies, diseases and more complex phototransduction processes can be difficult to model across the population of rods. While the single cell model can accurately reproduce voltage and current responses of an isolated photoreceptor, Kamiyama et al. [10] admitted

that perhaps a multi- compartment model might better express the flow of currents through the inner segment or synaptic terminal. However, we found this single cell model an adequate foundation model for our population model.

When modeling, assumptions must of course be made and are subject to critique. Our model is no exception. Presenting an image to our population of rods was an area which provided many assumptions.

We assumed the collecting area of a rod outer segment is uniformly  $0.43 \mu\text{m}^2$  across the population. Also, we assumed that every photon striking a rhodopsin activates that rhodopsin. Invergo et al. [5] used similar assumptions in the creation of their rod photoreceptor model. However, one half of photons traveling along a rod outer segment are absorbed. Furthermore, of that one half, an absorbed photon elicits rhodopsin activation and electrical response with a probability of two thirds [21]. We were keen to find how a rod population reacts after a rhodopsin has been activated, and therefore did not include these findings in our assumptions. Inclusion of these findings could allow for better description and modeling of the events that cause the phototransduction process across a rod population.

We assumed that the light intensity value striking the center of each cell represents the average strength of light cascading across the cell. Perhaps a better determination of the light value would involve finding the average light intensity. To find the average light intensity across an individual cell, calculation of the values striking the edges of the cell, as well as the center, would have been necessary. Only then could we calculate the average of these light intensities.

In both the hexagonal and Cartesian layout, we can simulate around 500 rod cells in a population. To expand our population model, and thus provide a closer estimate of the full retinal rod network in vertebrates, we need to develop high performance implementations.

### *4.3. Further Directions*

Future directions for study in this project include changing the vertebrate model to a mammalian model. Experimental studies on retinal dynamics are increasingly centered on mouse retina [22], thus converting the vertebrate model to a mammalian model would prove beneficial to the scientific community. Additionally, this study offers an opportunity to model rod photoreceptor diseases across a population. For example, with minimal modeling and some parameter adjustment, this model could provide quantitative description of diseases such as night blindness.

## 5. Acknowledgements

We thank University of Michigan for access to facilities and resources. Particular thanks to my mentor Dr. Adam Stinchcombe for his continual guidance. This study was supported by an NSF Grant (1045119).

## 6. References

- [1] J. I. Korenbrot, Speed, sensitivity, and stability of the light response in rod and cone photoreceptors: facts and models, *Progress in retinal and eye research* 31 (2012) 442–466.
- [2] D.-G. Luo, T. Xue, K. Yau, How vision begins: an odyssey, *Proceedings of the National Academy of Sciences* 105 (2008) 9855–9862.
- [3] D. Attwell, M. Wilson, S. M. Wu, The effect of light on the spread of signals through the rod network of the salamander retina, *Brain research* 343 (1985) 79–88.
- [4] V. Torre, et al., Model of phototransduction in retinal rods, *Cold Spring Harbor symposia on quantitative biology* 55 (1990).
- [5] B. M. Invergo, et al., A comprehensive model of the phototransduction cascade in mouse rod cells, *Molecular BioSystems* 10 (2014) 1481–1489.
- [6] D. Attwell, THE SHARPEYSCHAFER LECTURE ION CHANNELS AND SIGNAL PROCESSING IN THE OUTER RETINA, *Quarterly Journal of Experimental Physiology* 71 (1986) 496–536.
- [7] S. Barnes, B. Hille, Ionic channels of the inner segment of tiger salamander cone photoreceptors, *The Journal of General Physiology* 94 (1989) 719–743.
- [8] Y. Kamiyama, T. O’Sura, S. Usui, Ionic current model of the vertebrate rod photoreceptor, *Vision research* 36 (1996) 4059–4068.
- [9] S. Forti, et al., Kinetics of phototransduction in retinal rods of the newt *Titurus cristatus*, *The Journal of Physiology* 419 (1989) 265.
- [10] Y. Kamiyama, S. M. Wu, S. Usui, Simulation analysis of bandpass filtering properties of a rod photoreceptor network, *Vision research* 49 (2009) 970–978.
- [11] D. A. Baylor, M. G. F. Fuortes, P. M. O’bryan, Receptive fields of cones in the retina of the turtle, *The Journal of Physiology* 214 (1971) 265.

- [12] G. H. Gold, J. E. Dowling, Photoreceptor coupling in retina of the toa, *Bufo marinus* i. anatomy., *Journal of neurophysiology* 42 (1979) 292–310.
- [13] S. M. Wu, Synaptic transmission in the outer retina, *Annual Review of Physiology* 56 (1994) 141–168.
- [14] T. Lamb, E. Simon, The relation between intercellular coupling and electrical noise in turtle photoreceptors, *The Journal of Physiology* 263 (1976) 257–286.
- [15] N. G. Jin, et al., Rod electrical coupling is controlled by a circadian clock and dopamine in mouse retina, *The Journal of Physiology* 593 (2015) 1597–1631.
- [16] T. Guo, et al., Understanding the retina: A Review of Computational Models of the Retina from the Single Cell to the Network Level, *Critical Reviews in Biomedical Engineering* 42 (2014).
- [17] R. Hamer, et al., Multiple steps of phosphorylation of activated rhodopsin can account for the reproducibility of vertebrate rod single-photon responses, *The Journal of general physiology* 122 (2003) 419–444.
- [18] R. Hamer, et al., Toward a unified model of vertebrate rod phototransduction, *Visual neuroscience* 22 (2005) 417–436.
- [19] L. Shen, et al., Dynamics of mouse rod phototransduction and its sensitivity to variation of key parameters, *Systems Biology, IET* 4 (2010) 12–32.
- [20] C.-J. Jeon, et al., The Major Cell Populations of the Mouse Retina, *The Journal of Neuroscience* 18 (1998) 8936–8946.
- [21] F. Rieke, D. Baylor, Single-photon detection by rod cells of the retina, *Reviews of Modern Physics* 70 (1998) 1027.
- [22] A. D. Huberman, C. M. Niell, What can mice tell us about how vision works?, *Trends in neurosciences* 34 (2011) 464–473.

# Appendices

## A. Appendix A

Appendix A shows the single rod cell model introduced by Kamiyama et al. in 1996, 2009. It can be found in full detail [10].

Voltage membrane equation:

$$I_{all} = I_{photo} + I_h + I_{Kv} + I_{Ca} + I_{Cl(Ca)} + I_{K(Ca)} + I_L + I_{ex} + I_{ex2} \quad (1)$$

$$C_m \frac{dV}{dt} = -I_{all} \quad (2)$$

$$C_m = 0.02 \quad V(0) = -36.186 \quad (3)$$

Photocurrent model in [10], from [4]

$$\frac{dRh}{dt} = J_{hv} - \alpha_1 * Rh + \alpha_2 * Rh_i \quad (4)$$

$$\frac{dRh_i}{dt} = \alpha_1 * Rh - (\alpha_2 + \alpha_3) * Rh_i \quad (5)$$

$$\frac{dTr}{dt} = \epsilon * Rh * (T_{tot} - Tr) - \beta_1 * Tr + \tau_2 * PDE - \tau_1 * Tr * (PDE_{tot} - PDE) \quad (6)$$

$$\frac{dPDE}{dt} = \tau_1 * Tr * (PDE_{tot} - PDE) - \tau_2 * PDE \quad (7)$$

$$\frac{dCa}{dt} = b * J - \gamma_{Ca} * (Ca - C_0) - k_1 * (e_T - Cab) * Ca + k_2 * Cab \quad (8)$$

$$\frac{dCab}{dt} = k_1 * (e_T - Cab) * Ca - k_2 * Cab \quad (9)$$

$$\frac{dcGMP}{dt} = \frac{A_{max}}{1.0 + (Ca/Kc)^4} - cGMP * (\bar{V} + \sigma * PDE) \quad (10)$$

$$J = \frac{Jmax * (cGMP)^3}{cGMP^3 + 10^3} \quad (11)$$

$$I_{photo} = -J * \left(1.0 - \exp\left(\frac{V - 8.5}{17.0}\right)\right) \quad (12)$$

Delayed rectifier current ( $I_{Kv}$  [pA])

$$\alpha_{mKv} = \frac{5(100 - V)}{\exp\left(\frac{100 - V}{42}\right) - 1}, \beta_{mKv} = 9 \exp\left(-\frac{V - 20}{40}\right)$$

$$\alpha_{hKv} = 0.15 \exp\left(-\frac{V}{22}\right), \beta_{hKv} = \frac{0.4125}{\exp\left(\frac{10 - V}{7}\right) + 1}$$

$$\frac{dm_{Kv}}{dt} = \alpha_{mKv} \cdot (1 - m_{Kv}) - \beta_{mKv} \cdot m_{Kv} \cdot m_{Kv}(0) = 0.430$$

$$\frac{dh_{Kv}}{dt} = \alpha_{hKv} \cdot (1 - h_{Kv}) - \beta_{hKv} \cdot h_{Kv} \cdot h_{Kv}(0) = 0.999$$

$$I_{Kv} = \bar{g}_{Kv} \cdot m_{Kv}^3 \cdot h_{Kv} \cdot (V - E_K)$$

$$\bar{g}_{Kv} = 2.0 \text{ nS}, E_K = -74 \text{ mV}$$

Calcium current ( $I_{Ca}$  [pA])

$$\alpha_{mCa} = \frac{3(80 - V)}{\exp\left(\frac{80 - V}{25}\right) - 1}, \beta_{mCa} = \frac{10}{1 + \exp\left(\frac{V + 38}{7}\right)}, h_{Ca} = \frac{\exp\left(\frac{40 - V}{18}\right)}{1 + \exp\left(\frac{40 - V}{18}\right)}$$

$$\frac{dm_{Ca}}{dt} = \alpha_{mCa} \cdot (1 - m_{Ca}) - \beta_{mCa} \cdot m_{Ca} \cdot m_{Ca}(0) = 0.436$$

$$I_{Ca} = \bar{g}_{Ca} \cdot m_{Ca}^4 \cdot h_{Ca} \cdot (V - E_{Ca})$$

$$\bar{g}_{Ca} = 0.7 \text{ nS}, E_{Ca} = -12.5 \log\left(\frac{[Ca]_i}{[Ca]_o}\right), [Ca]_o = 1600 \mu\text{M}$$

Calcium-activated chloride current ( $I_{Cl(Ca)}$  [pA])

$$m_{Cl} = \frac{1}{1 + \exp\left(\frac{0.37 - [Ca]_i}{0.05}\right)}$$

$$I_{Cl(Ca)} = \bar{g}_{Cl} \cdot m_{Cl} \cdot (V - E_{Cl})$$

$$\bar{g}_{Cl} = 2.0 \text{ nS}, E_{Cl} = -20 \text{ mV}$$

Calcium-activated potassium current ( $I_{K(Ca)}$  [pA])

$$\alpha_{mKCa} = \frac{15(80 - V)}{\exp\left(\frac{80 - V}{40}\right) - 1}, \beta_{mKCa} = 20 \exp\left(-\frac{V}{35}\right)$$

$$\frac{dm_{KCa}}{dt} = \alpha_{mKCa} \cdot (1 - m_{KCa}) - \beta_{mKCa} \cdot m_{KCa} \cdot m_{KCa}(0) = 0.642$$

$$m_{KCa} = \frac{[Ca]_i}{[Ca]_i + 0.3}$$

$$I_{KCa} = \bar{g}_{KCa} \cdot m_{KCa}^2 \cdot m_{KCa} \cdot (V - E_K)$$

$$\bar{g}_{KCa} = 5.0 \text{ nS}, E_K = -74 \text{ mV}$$

Leakage current ( $I_L$  [pA])

$$I_L = g_L \cdot (V - E_L)$$

$$g_L = 0.35 \text{ nS}, E_L = -77 \text{ mV}$$

Figure 11: Ionic current Model from [10]

Intracellular calcium system ( $[Ca]_s$  [ $\mu\text{M}$ ])

$$\begin{aligned} \frac{d[Ca]_s}{dt} = & -\frac{I_{Ca} + I_{ex} + I_{ex2}}{2F \cdot V_1} \cdot 10^{-6} - D_{Ca} \frac{S_1}{\delta \cdot V_1} ([Ca]_s - [Ca]_f) \\ & - L_{b1} [Ca]_s (B_L - [Cab]_b) + L_{b2} [Cab]_b \\ & - H_{b1} [Ca]_s (B_H - [Cab]_{hs}) + H_{b2} [Cab]_{hs} \quad ([Ca]_s(0) = 0.0966) \end{aligned}$$

$$\begin{aligned} \frac{d[Ca]_f}{dt} = & D_{Ca} \frac{S_1}{\delta \cdot V_2} ([Ca]_s - [Ca]_f) - L_{b1} [Ca]_f (B_L - [Cab]_f) + L_{b2} [Cab]_f \\ & - H_{b1} [Ca]_f (B_H - [Cab]_{hf}) + H_{b2} [Cab]_{hf} \quad ([Ca]_f(0) = 0.0966) \end{aligned}$$

$$\frac{d[Cab]_b}{dt} = L_{b1} [Ca]_s (B_L - [Cab]_b) - L_{b2} [Cab]_b \quad ([Cab]_b(0) = 80.929)$$

$$\frac{d[Cab]_{hs}}{dt} = H_{b1} [Ca]_s (B_H - [Cab]_{hs}) - H_{b2} [Cab]_{hs} \quad ([Cab]_{hs}(0) = 29.068)$$

$$\frac{d[Cab]_f}{dt} = L_{b1} [Ca]_f (B_L - [Cab]_f) - L_{b2} [Cab]_f \quad ([Cab]_f(0) = 80.929)$$

$$\frac{d[Cab]_{hf}}{dt} = H_{b1} [Ca]_f (B_H - [Cab]_{hf}) - H_{b2} [Cab]_{hf} \quad ([Cab]_{hf}(0) = 29.068)$$

$$I_{ex} = J_{ex} \exp\left(-\frac{V + 14}{70}\right) \frac{[Ca]_s - Ca_e}{[Ca]_s - Ca_e + K_{ex}}, \quad I_{ex2} = J_{ex2} \frac{[Ca]_s - Ca_e}{[Ca]_s - Ca_e + K_{ex2}}$$

$$F = 9.648 \times 10^4 \text{ C mol}^{-1}, \quad V_1 = 3.812 \times 10^{-13} \text{ dm}^3,$$

$$V_2 = 5.236 \times 10^{-13} \text{ dm}^3, \quad D_{Ca} = 6 \times 10^{-8} \text{ dm}^2 \text{ s}^{-1},$$

$$\delta = 3 \times 10^{-5} \text{ dm}, \quad S_1 = 3.142 \times 10^{-8} \text{ dm}^2, \quad L_{b1} = 0.4 \text{ s}^{-1} \mu\text{M}^{-1},$$

$$L_{b2} = 0.2 \text{ s}^{-1}, \quad H_{b1} = 100 \text{ s}^{-1} \mu\text{M}^{-1}, \quad H_{b2} = 90 \text{ s}^{-1},$$

$$B_L = 500 \mu\text{M}, \quad B_H = 300 \mu\text{M}, \quad J_{ex} = 20 \text{ pA}, \quad J_{ex2} = 20 \text{ pA},$$

$$K_{ex} = 2.3 \mu\text{M}, \quad K_{ex2} = 0.5 \mu\text{M}, \quad Ca_e = 0.01 \mu\text{M}$$

Figure 12: Intracellular Calcium system from [10]